Journal of Biomedical Optics 5(2), 144–154 (April 2000)

Optical computed tomography in a turbid medium using early arriving photons

Kun Chen
Lev T. Perelman
Qingguo Zhang
Ramachandra R. Dasari
Michael S. Feld
Laser Biomedical Research Center
G. R. Harrison Spectroscopy Laboratory
Massachusetts Institute of Technology
Cambridge, Massachusetts 02139

Abstract. We employ photon migration to image absorbing objects embedded in a turbid medium. For improved resolution, we use early arriving photons (a few hundred picoseconds in excess of the time of flight), a regime in which the diffusion approximation breaks down. Our image reconstruction method is based on extension of x-ray computed tomography (CT) to the optical regime. The CT algorithm must be generalized to take into account the distributions of photon paths. We express the point spread function (PSF) in terms of the Green's function for the transport equation. This PSF then provides weighting functions for use in a generalized series expansion method of x-ray CT. Experiments were performed on a turbid medium with scattering and absorption properties similar to those of human breast tissue. Multiple absorbers were embedded into the medium to mimic tumors. Coaxial transmission scans were collected in two projections, and the early-time portions were analyzed. Through accurate modeling, we could remove the blurring associated with multiple scattering and obtain high-resolution images. Our results show that the diffusion approximation PSF is inadequate to describe the early arriving photons. A PSF incorporating causality is required to reconstruct accurate images of turbid media.
[S1083-3668(00)01202-8]

Keywords: photon migration; point spread function; early time detection; x-ray CT; optical CT.

Paper JBO-42015 received Sep. 15, 1999; revised manuscript received Feb. 4, 2000; accepted for publication Mar. 10, 2000.

1 Introduction

X-ray computed tomography (CT) has been very successful in imaging internal structures of the human body. It has provided an accurate, micron-resolution, real-time medical imaging tool for clinical use. However, the use of x rays has several disadvantages. The contrast is low for certain kinds of tumors, such as early stage breast cancer, the misdiagnosis rate for x-ray mammography is high, and x rays are mutagenic. In recent years, imaging techniques based on optical photons have attracted significant interest. In the spectral region between 700 and 900 nm, called the therapeutic window, photons do not give rise to mutagenic effects, and they can penetrate deep into tissues due to the weak absorption of light at these wavelengths. Sensitivity to optical contrast is high. Spectroscopic information can be obtained. Further, contrast can be enhanced by injecting exogenous dyes which target tumor cells.[1] Thus, the information provided by optical photons could complement that of x-ray CT, and perhaps provide an alternative diagnostic tool for detecting tumors and other abnormalities hidden deep inside the body.

The major obstacle to optical imaging is the high turbidity of human tissues. Photons injected into tissue undergo multiple scattering events before they are detected. To extract spatial information, one has to disentangle the effects of scattering. Various optical imaging approaches have been developed to deal with this problem. Significant research has been carried out using frequency-domain imaging,[2,3] time-resolved imaging,[4–6] continuous wave (cw) imaging,[7] diffraction tomographic imaging,[8] and imaging based on microscopic Beer–Lambert law.[9] Each of these approaches has advantages and disadvantages. Imaging techniques utilizing ballistic photons, which are very good for imaging up to 1 mm inside the tissue, do not work in the case of deep tissue imaging. Several image reconstruction schemes have been devised to deconvolve turbidity and improve spatial resolution. Finite element methods and finite difference methods have been developed in the time domain[10] and the frequency domain,[11] respectively. Filtered backprojection has been applied to cw imaging.[7] Weighting factors for the contribution of individual voxels to the measurement, first proposed in x-ray CT,[12] have also been calculated using Monte Carlo simulations and are employed in the inverse model.[13,14] In this article we demonstrate a way to extend the series expansion methods of x-ray CT to the optical regime. Using an early time detection approach, we are able to create a sharp three-dimensional (3D) image of a tissue-like turbid medium and correct for the effects of turbidity.

Important insight into this problem can be obtained by comparing the propagation of optical and x-ray photons in human tissue. The photon path concept plays a key role here. As is well known, x rays traversing the body [Figure 1(a)]

Address all correspondence to Michael S. Feld. Tel: 617-253-7700; Fax: 617-253-4513; E-mail: msfeld@mit.edu

1083-3668/2000/$15.00 © 2000 SPIE

travel along straight lines. In contrast, due to scattering, the propagation of optical photons has a 3D spread. The distribution of optical photon paths can be visualized as a tube connecting the source and the detector [Figure 1(b)]. The width of the cross section of the tube varies according to the time at which arriving photons are collected.

Several features of the photon path distribution are noted below.

1. In the time-of-flight limit this tube reduces to a straight line, and the problem is reduced to that of conventional x-ray CT. However the signal produced by these so-called ballistic photons is extremely weak and essentially nondetectable for thick tissues.
2. For early detection times (a few hundred ps after the time of flight), the tube is still very narrow and the photon paths are well defined. The transmitted signals are significant, and spatial information is still highly preserved.
3. At late detection times (several ns), the tube can completely fill the organ of interest, and spatial resolution is significantly reduced. We refer to this regime as the diffusive limit.

Physical intuition suggests that, if we replace the straight line paths of x rays with the narrow tubes of the early time photon path distribution, we can construct an optical CT algorithm which is only a slight modification of that used in x-ray CT. In fact, as we demonstrate in this article, the mathematical formulation of optical CT has strong similarities to that of x-ray CT.

2 Mathematical Basis: Theoretical Models

The mathematical description of the attenuation of the x-ray intensity through the human body is well established. Assume the human tissue under study has an absorption distribution $\mu_a^X(\mathbf{r}')$ for a monochromatic x ray. Then the transmitted intensity of the x-ray beam across the body is

$$I(\mathbf{r}) = I_0 \exp\left[- \int_{\mathbf{r}_0}^{\mathbf{r}} dl\, \mu_a^X(\mathbf{r}') \right], \tag{1}$$

where the integral is along the straight line connecting the source at $\mathbf{r}_0$ and the detector at $\mathbf{r}$. Equation (1) can be rewritten as

$$-[\ln I(\mathbf{r}) - \ln I_0] = \int_{\mathbf{r}_0}^{\mathbf{r}} dl\, \mu_a^X(\mathbf{r}'). \tag{2}$$

The above line integral is often referred to as the Radon transform.[12]

Unlike x rays, near infrared light in human tissue undergoes strong scattering and does not follow straight line paths. Optical photons undergo multiple scattering events before they are detected or absorbed by the tissue. The distribution of photon paths in a uniform scattering medium has been studied using various approaches.[15–19] It has been established that the distribution of the photon paths is narrow at early detection times, but spreads out as the time increases.

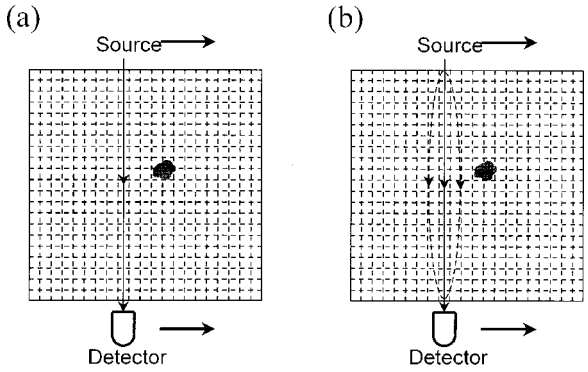

Fig. 1 Schematic diagram extending the ART for x-ray CT to optical CT. The sample under study is divided into $N \times N \times N$ voxels. The absorption distribution is represented by the average absorption within each voxel.

Generally, the presence of tumors creates optical anisotropy which appears as a local variation of the scattering and the absorption properties of the tissue. For early stage tumors, these changes can be considered as small perturbations.

The propagation of near infrared photons in human tissue is described well by the transport equation.[20,21] For a medium with scattering distribution $\mu_s(\mathbf{r})$ and absorption distribution $\mu_a(\mathbf{r})$, the radiance $L(\mathbf{r},\hat{s},t)$ satisfies

$$\begin{aligned} \frac{1}{c}\frac{\partial L(\mathbf{r},\hat{s},t)}{\partial t} + \hat{s}\cdot\nabla L(\mathbf{r},\hat{s},t) &= -[\mu_a(\mathbf{r}) + \mu_s(\mathbf{r})] L(\mathbf{r},\hat{s},t) \\ &\quad + \mu_s(\mathbf{r}) \int_{4\pi}\int L(\mathbf{r},\hat{s}',t) f_{\mathbf{r}}(\hat{s}\cdot\hat{s}')\, d\Omega' + Q(\mathbf{r},\hat{s},t). \end{aligned} \tag{3}$$

and the normalized differential scattering cross section $f_{\mathbf{r}}(\hat{s}\cdot\hat{s}')$, often referred to as the phase function, satisfies

$$\int_{4\pi}\int f_{\mathbf{r}}(\hat{s}\cdot\hat{s}')\, d\Omega' = 1. \tag{4}$$

In Eq. (3), c is the speed of light in the medium, and $Q(\mathbf{r},\hat{s},t)$ is the source term. For a perturbative system, the distribution of absorption, scattering, and phase function have small variations of the form

$$\begin{aligned} \mu_a(\mathbf{r}) &= \mu_a + \delta\mu_a(\mathbf{r}), \\ \mu_s(\mathbf{r}) &= \mu_s + \delta\mu_s(\mathbf{r}), \\ \mu_s(\mathbf{r}) f_{\mathbf{r}}(\hat{s}\cdot\hat{s}') &= \mu_s f(\hat{s}\cdot\hat{s}') + \delta\tilde{\mu}_s(\mathbf{r},\hat{s}\cdot\hat{s}'), \end{aligned} \tag{5}$$

with

$$\delta\tilde{\mu}_s(\mathbf{r},\hat{s}\cdot\hat{s}') = \delta\mu_s(\mathbf{r}) f_{\mathbf{r}}(\hat{s}\cdot\hat{s}') + \mu_s[f_{\mathbf{r}}(\hat{s}\cdot\hat{s}') - f(\hat{s}\cdot\hat{s}')].$$

In Eq. (5), μ_a and μ_s are the average absorption and scattering coefficients, respectively; $\delta\mu_a(\mathbf{r})$ ($\ll\mu_a$) and $\delta\mu_s(\mathbf{r})$ ($\ll\mu_s$) are the perturbations caused by the tumors. Generally, the local variation of the phase function $f_{\mathbf{r}}(\hat{s}\cdot\hat{s}')$ from the global phase function $f(\hat{s}\cdot\hat{s}')$ may not be small for some

angles, but Eq. (4) requires that such variations cancel each other after integrating over all solid angles. So we can treat $\delta\tilde{\mu}_s(\mathbf{r},\hat{s}\cdot\hat{s}')$ as a small perturbation.

Under variations given by Eq. (5), Eq. (3) can be solved using perturbation theory. For the case of a point source,

$$Q(\mathbf{r},\hat{s},t)=\delta(\mathbf{r}-\mathbf{r}_0)\,\delta(t-t_0), \tag{6}$$

Eq. (3) is the equation for the Green's function $G_{\hat{s}}(\mathbf{r},t|\mathbf{r}_0,t_0)$, which has an expansion

$$G_{\hat{s}}(\mathbf{r},t|\mathbf{r}_0,t_0)=G_{\hat{s}}^{(0)}(\mathbf{r},t|\mathbf{r}_0,t_0)+G_{\hat{s}}^{(1)}(\mathbf{r},t|\mathbf{r},t_0)+\ldots, \tag{7}$$

with $G_{\hat{s}}^{(0)}(\mathbf{r},t|\mathbf{r}_0,t_0)$ the normal Green's function in the absence of perturbation and $G_{\hat{s}}^{(1)}(\mathbf{r},t|\mathbf{r}_0,t_0)$ the first order correction due to the perturbation. Substituting Eqs. (5)–(7) into Eq. (3) and keeping terms only up to the first order, we have

$$\begin{aligned}
&\frac{1}{c}\frac{\partial G_{\hat{s}}^{(0)}(\mathbf{r},t|\mathbf{r}_0,t_0)}{\partial t}+\hat{s}\cdot\nabla G_{\hat{s}}^{(0)}(\mathbf{r},t|\mathbf{r}_0,t_0)+(\mu_a+\mu_s)\\
&\quad\times G_{\hat{s}}^{(0)}(\mathbf{r},t|\mathbf{r}_0,t_0)-\mu_s\int\int_{4\pi} G_{\hat{s}'}^{(0)}(\mathbf{r},t|\mathbf{r}_0,t_0)f(\hat{s}\cdot\hat{s}')d\Omega'\\
&\quad=\delta(\mathbf{r}-\mathbf{r}_0)\,\delta(t-t_0),
\end{aligned} \tag{8}$$

and

$$\begin{aligned}
&\frac{1}{c}\frac{\partial G_{\hat{s}}^{(1)}(\mathbf{r},t|\mathbf{r},t_0)}{\partial t}+\hat{s}\cdot\nabla G_{\hat{s}}^{(1)}(\mathbf{r},t|\mathbf{r}_0,t_0)+(\mu_a+\mu_s)\\
&\quad\times G_{\hat{s}}^{(1)}(\mathbf{r},t|\mathbf{r}_0,t_0)-\mu_s\int\int_{4\pi} G_{\hat{s}'}^{(1)}(\mathbf{r},t|\mathbf{r}_0,t_0)f(\hat{s}\cdot\hat{s}')d\Omega'\\
&\quad=-[\delta\mu_a(\mathbf{r})+\delta\mu_s(\mathbf{r})]G_{\hat{s}}^{(0)}(\mathbf{r},t|\mathbf{r}_0,t_0)\\
&\qquad+\int\int_{4\pi} G_{\hat{s}'}^{(0)}(\mathbf{r},t|\mathbf{r}_0,t_0)\,\delta\tilde{\mu}_s(\mathbf{r},\hat{s}\cdot\hat{s}')d\Omega'.
\end{aligned} \tag{9}$$

Equation (9) can be solved through the adjoint equation of Eq. (8), which is

$$\begin{aligned}
&-\frac{1}{c}\frac{\partial G_{\hat{s}}^{(0)}(\mathbf{r},t|\mathbf{r}_0,t_0)}{\partial t_0}-\hat{s}\cdot\nabla_0 G_{\hat{s}}^{(0)}(\mathbf{r},t|\mathbf{r}_0,t_0)\\
&\quad+(\mu_a+\mu_s)G_{\hat{s}}^{(0)}(\mathbf{r},t|\mathbf{r}_0,t_0)\\
&\quad-\mu_s\int\int_{4\pi} G_{\hat{s}'}^{(0)}(\mathbf{r},t|\mathbf{r}_0,t_0)f(\hat{s}\cdot\hat{s}')d\Omega'\\
&\quad=\delta(\mathbf{r}-\mathbf{r}_0)\,\delta(t-t_0).
\end{aligned} \tag{10}$$

It can be shown[22] that the solution to Eq. (9) satisfies

$$\begin{aligned}
&\int\int_{4\pi} d\Omega G_{\hat{s}}^{(1)}(\mathbf{r},t|\mathbf{r}_0,t_0)\\
&\quad=-\int_{-\infty}^{t^+}dt'\int d^3\mathbf{r}'[\delta\mu_a(\mathbf{r}')+\delta\mu_s(\mathbf{r}')]\\
&\qquad\times\int\int_{4\pi} d\Omega G_{\hat{s}}^{(0)}(\mathbf{r},t|\mathbf{r}',t')G_{\hat{s}}^{(0)}(\mathbf{r}',t'|\mathbf{r}_0,t_0)\\
&\qquad+\int_{-\infty}^{t^+}dt'\int d^3\mathbf{r}'\int\int_{4\pi} d\Omega\int\int_{4\pi} d\Omega' G_{\hat{s}}^{(0)}(\mathbf{r},t|\mathbf{r}',t')\\
&\qquad\times G_{\hat{s}'}^{(0)}(\mathbf{r}',t'|\mathbf{r}_0,t_0)\,\delta\tilde{\mu}_s(\mathbf{r}',\hat{s}\cdot\hat{s}')-\int_{-\infty}^{t^+}dt'\oint_{\partial V} d\mathbf{A}'\\
&\qquad\cdot\int\int_{4\pi} d\Omega\hat{s}G_{\hat{s}}^{(0)}(\mathbf{r},t|\mathbf{r}',t')\\
&\qquad\times G_{\hat{s}}^{(1)}(\mathbf{r}',t'|\mathbf{r}_0,t_0).
\end{aligned} \tag{11}$$

Under the assumption of uniqueness of the solution to the transport equation, Eq. (11) can be reduced to

$$\begin{aligned}
G_{\hat{s}}^{(1)}(\mathbf{r},t|\mathbf{r}_0,t_0)=&-\int_{-\infty}^{t^+}dt'\int d^3\mathbf{r}'\,\delta\mu_a(\mathbf{r}')G_{\hat{s}}^{(0)}(\mathbf{r},t|\mathbf{r}',t')\\
&\times G_{\hat{s}}^{(0)}(\mathbf{r}',t'|\mathbf{r}_0,t_0)-\int_{-\infty}^{t^+}dt'\int d^3\mathbf{r}'\,\delta\mu_s(\mathbf{r}')\\
&\times G_{\hat{s}}^{(0)}(\mathbf{r},t|\mathbf{r}',t')G_{\hat{s}}^{(0)}(\mathbf{r}',t'|\mathbf{r}_0,t_0)\\
&+\int_{-\infty}^{t^+}dt'\int d^3\mathbf{r}'\int\int_{4\pi} d\Omega' G_{\hat{s}}^{(0)}(\mathbf{r},t|\mathbf{r}',t')\\
&\times G_{\hat{s}'}^{(0)}(\mathbf{r}',t'|\mathbf{r}_0,t_0)\,\delta\tilde{\mu}_s(\mathbf{r}',\hat{s}\hat{s}')\\
&-\int_{-\infty}^{t^+}dt'\oint_{\partial V} d\mathbf{A}'\cdot\int\int_{4\pi} d\Omega\hat{s}G_{\hat{s}}^{(0)}(\mathbf{r},t|\mathbf{r}',t')\\
&\times G_{\hat{s}}^{(1)}(\mathbf{r}',t'|\mathbf{r}_0,t_0).
\end{aligned} \tag{12}$$

The first term on the right-hand side (rhs) of Eq. (12) is the correction due to absorption variations, the second and the third terms contain the correction due to scattering variations; the third term also includes an extra correction due to phase function variations. The last term in Eq. (12) is the surface integral and is related to the boundary condition. For boundary conditions commonly used, such as the zero-boundary condition[23] in our model described below, the surface integral contributes at higher order and can be ignored. Since in this article we will only focus on absorption-based imaging, we shall discuss the first term only. Discussion of the other terms, which are relevant to scattering and phase function variations, will be treated elsewhere. In order to simplify the formulation, we define the point spread function as

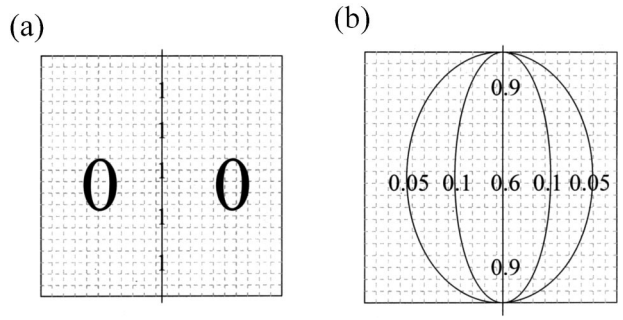

Fig. 2 Each voxel is assigned a weighting factor. For the x ray, the voxel on the trajectory contributes 100%, while off the trajectory contributes 0%. For optical photons, the weighting factor is determined by the photon path distribution.

$$\text{PSF}\ (\mathbf{r},t;\mathbf{r}';\mathbf{r}_0,t_0)=\int_{-\infty}^{t^+}dt'\,G_{\hat{s}}^{(0)}(\mathbf{r},t|\mathbf{r}',t') \times G_{\hat{s}}^{(0)}(\mathbf{r}',t'|\mathbf{r}_0,t_0). \tag{13}$$

Therefore, Eqs. (7) and (12) can be rewritten as

$$-[G_{\hat{s}}(\mathbf{r},t|\mathbf{r}_0,t_0)-G_{\hat{s}}^{(0)}(\mathbf{r},t|\mathbf{r}_0,t_0)] = \int d^3\mathbf{r}'\,\delta\mu_a(\mathbf{r}')\ \text{PSF}\ (\mathbf{r},t;\mathbf{r}';\mathbf{r}_0,t_0). \tag{14}$$

We note the remarkable similarity between Eqs. (2) and (14). Physically, PSF $(\mathbf{r},t;\mathbf{r}';\mathbf{r}_0,t_0)$ is the probability that a photon is injected at the source point $\mathbf{r}_0$ at time t_0, passes through the field point $\mathbf{r}'$ before time t, and is collected by the detector at point $\mathbf{r}$ at time t. It represents the photon path distribution at time t between the light source and the detector. In the ballistic limit, the photon path distribution in the transverse direction (i.e., the direction perpendicular to $\mathbf{r}-\mathbf{r}_0$) shrinks to a δ function:

$$\text{PSF}\ (\mathbf{r},t;\mathbf{r}';\mathbf{r}_0,0)\xrightarrow{t\to|\mathbf{r}-\mathbf{r}_0|/c}\delta^{\perp}(\mathbf{r}-\mathbf{r}_0).$$

Thus, the volume integral on the rhs of Eq. (14) reduces to a line integral along $\mathbf{r}-\mathbf{r}_0$, and Eqs. (2) and (14) are essentially identical.

It is important to note that the derivation of Eq. (14) does not use assumptions of the diffusion approximation. The Green's function $G_{\hat{s}}^{(0)}(\mathbf{r},t|\mathbf{r}',t')$ in Eq. (13) can be calculated using various theoretical models. Three examples are the path integral solutions,[16,17] the random walk solution,[18] and the conventional diffusion approximation solution.[20,23] In fact, our reconstruction results below show that the conventional diffusion solution is inadequate for imaging with early arriving photons. It predicts a point spread function that is too wide and renders images that are too small. A solution satisfying causality is required.

For the purpose of comparison, we introduce the diffusion approximation[20]

$$G_{\hat{s}}^{(0)}(\mathbf{r},t|\mathbf{r}_0,t_0)\cong G^{(0)}(\mathbf{r},t|\mathbf{r}_0,t_0)-\frac{1}{\mu_{\text{tr}}}\hat{s}\cdot\nabla G^{(0)}(\mathbf{r},t|\mathbf{r}_0,t_0)$$

$$G_{\hat{s}}^{(1)}(\mathbf{r},t|\mathbf{r}_0,t_0)\cong G^{(1)}(\mathbf{r},t|\mathbf{r}_0,t_0)-\frac{1}{\mu_{\text{tr}}}\hat{s}\cdot\nabla G^{(1)}(\mathbf{r},t|\mathbf{r}_0,t_0),$$

where μ_{tr} is the transport scattering property defined as $\mu_{\text{tr}}=\mu_a+\mu_s'$, and $\mu_s'=(1-g)\mu_s$ with g the mean cosine of the forward scattering angle. It can be shown from Eq. (11) that the first order correction to the Green's function is

$$\begin{aligned}G^{(1)}(\mathbf{r},t|\mathbf{r}_0,t_0)=&-\int d^3\mathbf{r}'\,\delta\mu_a(\mathbf{r}')\int_{-\infty}^{t^+}dt'\\ &\times\Big[G^{(0)}(\mathbf{r},t|\mathbf{r}',t')G^{(0)}(\mathbf{r}',t'|\mathbf{r}_0,t_0)\\ &+\frac{1}{3\mu_{\text{tr}}^2}\nabla G^{(0)}(\mathbf{r},t|\mathbf{r}',t')\cdot\nabla' G^{(0)}\\ &\times(\mathbf{r}',t'|\mathbf{r}_0,t_0)\Big]\\ &-\frac{1}{3\mu_{\text{tr}}^2}\int d^3\mathbf{r}'\,\delta\mu_s'(\mathbf{r}')\int_{-\infty}^{t^+}dt'\\ &\times\nabla G^{(0)}(\mathbf{r},t|\mathbf{r}',t')\cdot\nabla' G^{(0)}(\mathbf{r}',t'|\mathbf{r}_0,t_0).\end{aligned}$$

The above equation is identical to the correction calculated directly from the diffusion equation with perturbation theory.[24]

3 Inverse Procedure

We now briefly discuss the series expansion method and the algebraic reconstruction technique (ART) for x-ray CT.[12,25] The volume to be imaged is split into $N\times N\times N$ cubic voxels. Each voxel is assigned a value that represents the local average of the absorption distribution. The imaging problem is two dimensional (2D) in the case of x rays. The linear attenuation in Eq. (2) is then simplified to a summation of the voxel values along the source–detector line. The ray sum can be exactly expressed as

$$y_j=\sum_{i=1}^{N^2}b_{ij}w_{ij}\mu_i. \tag{15}$$

In Eq. (15), y_j is the data of the jth measurement; w_{ij} is a geometric factor related to the oblique angle of the jth measurement, and it equals the segment length of the jth ray within voxel i; μ_i is the local average of the absorption within voxel i. The summation on the right-hand side of Eq. (15) is that of the N^2 voxels on the detection plane because of the linear transmitter assumption for x rays. In the case of x rays, the factor b_{ij} is given as

$$b_{ij}=\begin{cases}1, & \text{the } j\text{th ray crosses pixel } i;\\ 0, & \text{other.}\end{cases} \tag{16}$$

As illustrated in Figure 2(a), through the introduction of the weighting factor b_{ij}, the plane summation in Eq. (15) is ac-

tually a line summation. Those voxels that fall on the line contribute 100% to the x-ray function, while those that fall away from the line contribute 0%.

Our extension to optical CT is through the weighting factor b_{ij}. Because of scattering, photons have different probabilities to follow different paths. Therefore, the contribution of each voxel to a source–detector measurement is weighted by the density of photon paths across it. The natural choice of b_{ij} for the optical case is the value of the photon path probability [Figure 2(b)]; Eq. (15) can then be directly applied. Recalling that the photon path is a 3D tube, summation over three dimensions is required. The generalized equation is

$$y_j = \sum_{i=1}^{N^3} b_{ij} w_{ij} \langle \delta\mu_a \rangle_i . \tag{17}$$

This is exactly the discrete form of Eq. (14) at a fixed time t if we set

$$y_j = -[G_{\hat{s}}(\mathbf{r}_j, t|\mathbf{r}_0, t_0) - G_{\hat{s}}^{(0)}(\mathbf{r}_j, t|\mathbf{r}_0, t_0)],$$

$$\langle \delta\mu_a \rangle_i = \delta\mu_a(\mathbf{r}_i), \tag{18}$$

$$b_{ij} w_{ij} = \mathrm{PSF}(\mathbf{r}_j, t; \mathbf{r}_i; \mathbf{r}_0, 0)\Delta \mathrm{v},$$

with Δv the volume element of each voxel. Equation (17) can be rewritten in compact matrix form as

$$\mathbf{y} = \mathbf{R}\mathbf{x} + \mathbf{n}, \tag{19}$$

where $\mathbf{y}$ is the measurement vector (dimension M), $\mathbf{x}$ is the image vector (dimension N^3), $\mathbf{R}$ is the projection matrix containing geometric and photon path information (dimension $M \times N^3$), and $\mathbf{n}$ denotes the error vector.

In our image reconstructions, we apply the additive ART of x-ray CT directly to optical CT. Since the imaging problem can be either overdetermined or underdetermined, it is inappropriate to solve the equation $\mathbf{y} = \mathbf{R}\mathbf{x}$ directly since it may not have any solution at all, or it may have many solutions but none is appropriate. Estimation of the image vector is usually performed using optimization criteria based on the error between forward model predictions and experimental data, as well as *a priori* information about the imaging region. One example is the so-called regularized least-squares criterion, which is a special case of the Bayesian estimate. Reconstruction of the sought-after image is performed through minimizing the function,

$$r^2 \|\mathbf{y} - \mathbf{R}\mathbf{x}\|^2 + \|\mathbf{x} - \delta\mu_0\|^2. \tag{20}$$

In Eq. (20), r is a parameter often called the signal-to-noise ratio[12,25] in the literature, $\delta\mu_0$ is the pre-knowledge of the image vector ($N^3 \times 1$) and also used as the initial estimate of the image, and $\|\cdots\|^2$ denotes the module square for the vector. Keeping the second term small ensures that the picture is not too far from the pre-knowledge, and keeping the first term small ensures that the picture is consistent with the measurements.

One iterative procedure[25] to minimize Eq. (20) is to introduce two sequences of vectors, $\mathbf{x}^{(k)}$ and $\mathbf{u}^{(k)}$, of dimensions N^3 and M, respectively. Initially, $\mathbf{x}^{(0)}$ is set equal to $\delta\mu_0$ and $\mathbf{u}^{(0)}$ to a zero vector. The iterative step is given by

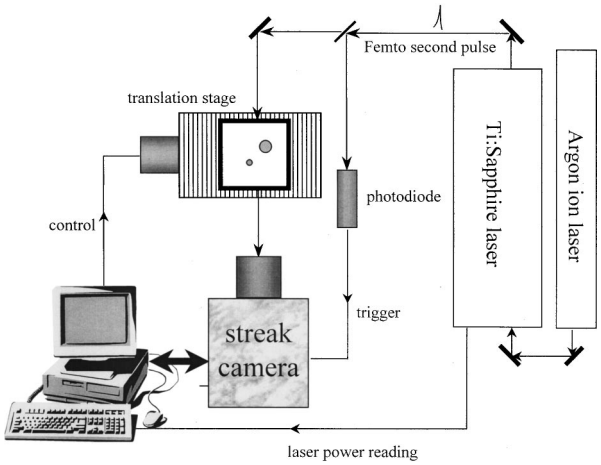

Fig. 3 Schematic diagram of the experiment setup.

$$\begin{aligned} \mathbf{x}^{(k+1)} &= \mathbf{x}^{(k)} + r c^{(k)} \mathbf{R}_{i_k} \\ \mathbf{u}^{(k+1)} &= \mathbf{u}^{(k)} + c^{(k)} \mathbf{e}_{i_k}, \end{aligned} \tag{21}$$

where

$$c^{(k)} = \lambda \frac{r\left(y_{i_k} - \sum_{j=1}^{N^3} R_{i_k,j} x_j^{(k)} \right) - u_{i_k}^{(k)}}{1 + r^2 \|R_{i_k}\|^2}, \tag{22}$$

with $i_k = k(\mathrm{mod}\, N^3) + 1$, R_i the transpose of the ith row of the matrix $\mathbf{R}$, e_i the M dimensional column vector with 1 in the ith row and 0 elsewhere, and λ is a real number called the relaxation parameter.[25] It has been proven that as long as $0 < \lambda < 2$ the sequence $\{x^{(k)}\}$ converges in the limit to the minimizer of Eq. (20).

4 Experimental Setup

In order to demonstrate this new optical CT technique, we conducted experiments in a cubic glass container 6.35 cm on each side, filled with a tissue-like scattering medium. Cubic geometry was selected to simplify theoretical modeling because of its regular boundaries. The scattering medium was a stock solution prepared with 1.072 μm diam polystyrene beads (PolyScience, Inc.) at 0.27% concentration. The scattering and absorption properties of the medium were determined in real time by fitting the transmitted diffuse light.[23] A schematic diagram of the setup is presented in Figure 3. The light source was a Coherent Mira 900 mode-locked Ti:sapphire laser operated in femtosecond mode and pumped by a Coherent Innova 400 multiline argon ion laser. The wavelength was 800 nm, and the repetition rate was 76 MHz. The pulse width was ~150 fs. The detection system was a Hamamatsu C5680 streak camera with a M5675 synchroscan unit. A small portion of the laser beam was deflected by a quartz plate to a fast photodiode (Hamamatsu C1808-02), which generates the triggering signal for the streak camera. The cubic glass container was mounted on a translation stage. A Pentium-II computer served as a central control and data acquisition unit. In order to monitor the laser power drift during the scan, a DT2801-A card (Data Translation, Inc.) was installed on the computer

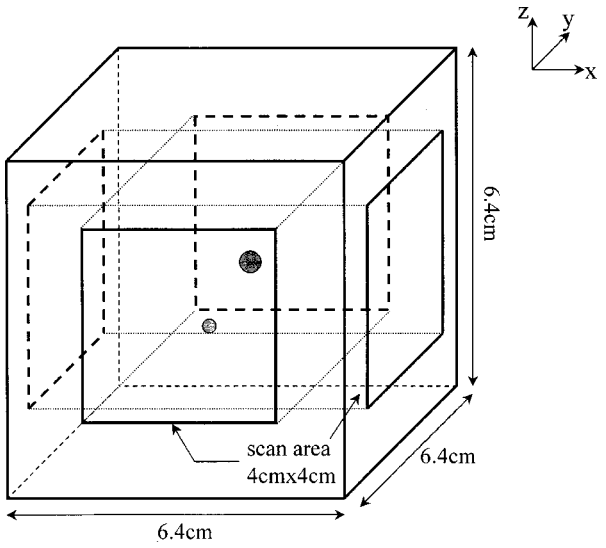

Fig. 4 Dimension of the scattering medium and the scanning geometry.

and programmed to record the laser power voltage from the control box of the Mira 900, and it also served to drive the stepper motor of the translation stage. Total automation of data acquisition for a full line scan was achieved by programming the user interface of the streak camera software. The streak camera was operated in analog mode. It converted the temporal evolution of light signals into vertical streak images. The transmitted light was collected with four coherent fiber bundles (Sumitomo, Ltd.). Each fiber bundle had a 500 μm core diameter and consisted of 10 000 single mode silica fibers. The proximal ends of the four fibers were bundled together to increase the collection area. The overall time resolution of the detection system was set to 30 ps.

The container was placed in the sample holder on the translation stage. Multiple objects were embedded inside the turbid medium at fixed positions. The sample holder was designed so that the top, bottom, and left and right boundaries of the container were totally black. The laser pulses were delivered into the medium at the front side, and the transmitted signals were collected at the opposite side. The incoming laser beam and the collection fibers were aligned in a coaxial geometry. Surface scans were conducted on the *XZ* and *YZ* directions (see Figure 4), so that a 3D image of the absorption distribution could be reconstructed. The scan area was a 4 cm$\times$4 cm square along each direction. The scans were 2 mm per step in the horizontal and vertical directions, resulting in 2 projections, 882 total scan measurements. The data acquisition time for each point was 8 s. Either one or two opaque objects were embedded into the medium. In each case, the scans were first carried out for the *XZ* plane, and then the container was rotated 90° and the scans were continued for the *YZ* plane.

5 Experimental Results and Reconstructed Images

Calculation of the point spread function requires knowledge about the average scattering and absorption properties of the scattering medium (μ_s' and μ_a). To determine μ_s' and μ_a, we collected the coaxial transmission signal of a 2.2 ns time window, with the absorbers removed from the scattering medium and the source detector aligned at the center of the *X* surface. We then fitted this time-dependent curve using the diffusion approximation solution with zero-boundary condition.[23] The best fit was given by $\mu_s'=7.38\,\mathrm{cm}^{-1}$ and $\mu_a=0.03\,\mathrm{cm}^{-1}$. These values are similar to those of human breast tissue.

In our experiments, we collected data for two configurations. In the first case, an 8 mm diam black sphere was placed at the center of the container (a one object configuration). In the second case, a black sphere 8 mm in diameter was placed (0.56, 0.56, -0.56) cm from the center, and a second black sphere 6 mm in diameter was placed (-0.56, -0.56, 0.56) cm from the center (a two object configuration). For each case, scanning was performed on the surfaces in 2 mm steps, and 882 time evolution curves of the transmission signals were measured, one for each scanning point. Because the source–detector distance remained the same for all 882 measurements, the time scale was the same and the intensities can be compared at the same time point. When the source–detector line crosses the absorber, we should see a drop in signal level, and vice versa. Projection intensity diagrams can be easily created by plotting the contour map of the intensities of all 882 time evolution curves at the same time point. To achieve higher counts and reduce noise, these intensities can be summations of counts over a time window comparable to the time resolution of the detecting system. The selection of the time point is based on a trade-off between spatial resolution and the signal-to-noise level. The early time portion has better spatial resolution, but the low signal level suffers from relatively higher noise and will distort the image. The later time portion has a higher signal level, but the spatial resolution goes down. The time windows for summation selected are the following: for the one object configuration, we choose 534–600 ps as the time window; for the two object configuration, we choose 607–657 ps as the time window. Here time zero is the time of flight. The projection intensity diagrams are presented in Figure 5. As expected, the projection lines crossing the absorbers have weaker intensity. The absorbers appear as shadows on the projection intensity diagrams. The projections of one embedded absorber [Figures 5(a) and 5(b)] are different from those of two embedded absorbers [Figures 5(c) and 5(d)]. Figures 5(a)–5(d) are referred to as the zeroth order images. They already show features such as the central positions of the embedded objects, although the images are scrambled due to scattering.

Before processing the data in Figure 5, artifacts at the edges due to tiny air bubbles and asymmetry of the surface were removed manually, and a grid was created. In our analysis we chose a 2 mm scanning step as the size of each grid, resulting in $21^3=9261$ voxels. The inverse is underdetermined since we want to reconstruct 9261 voxel values from 882 measurements.

The image reconstruction algorithm was then applied in two steps. First, the straight line PSF of x-ray CT was applied to the data using ART [Eqs. (21) and (22)] with an initial guess of $\boldsymbol{\delta\mu}_0=\mathbf{0}$ [see Eq. (20)] and signal-to-noise ratio $r=60$. Second, the resulting image, obtained with the straight line PSF, was then used as an initial guess and applied to the data using a particular photon migration PSF. The signal-to-

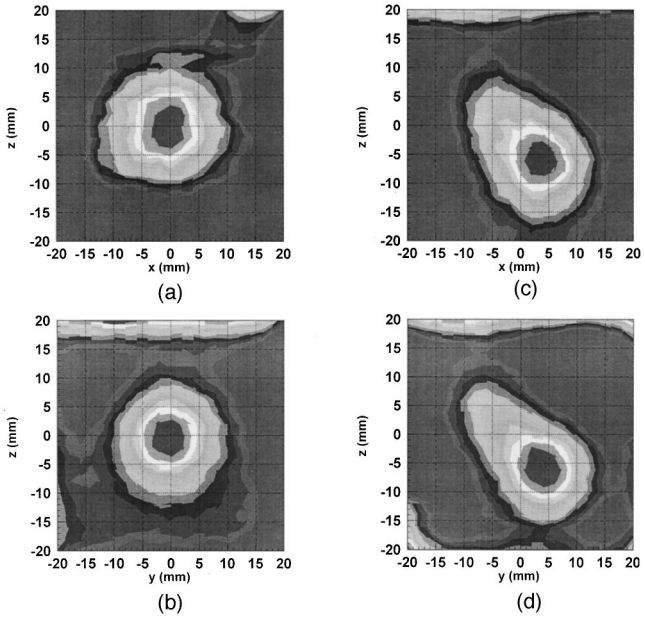

Fig. 5 Contour map of the intensities for (a), (b) one object and (c), (d) two objects. The time windows are at $\Delta t = 534$ ps, width 50 ps for (a), (b) and $\Delta t = 607$ ps, width 50 ps for (c), (d).

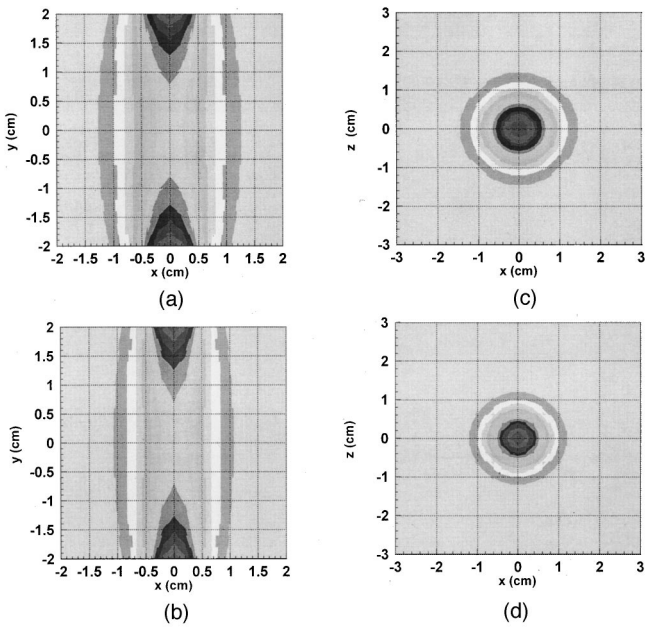

Fig. 6 Point spread functions. The source and detector are at (0, −3.2, 0) and (0, 3.2, 0) cm, respectively. Four combinations are given. (a) Side view of the $z = 0$ plane, calculated with the diffusion approximation; (b) side view of the $z = 0$ plane, calculated with the causality correction; (c) top view of the $y = 0$ plane, calculated with the diffusion approximation; (d) top view of the $y = 0$ plane, calculated with the causality correction. Note that the point spread function calculated using the diffusion approximation solution is wider than that using the causality corrected solution.

noise ratio in Eq. (20) was again set to $r = 60$, and the relaxation parameter in Eq. (22) was set to $\lambda = 1$. The reconstructions were computed with point spread functions calculated from both the diffusion approximation[20] and the causality corrected solutions[18] (see below). The number of iteration steps was set to 2×10^5. On a Pentium-II 450 MHz PC, each reconstruction took ~40 s. We increased the number of iteration steps to 2×10^6 without observing much improvement.

The second step involves the calculation of the PSF from solutions to the transport equation. The diffusion approximation solution is widely used in the literature. However, it is well known that this solution violates causality and breaks down in the early time regime. Solutions incorporating causality have been worked out for models based on random walk[18] and path integral[16,17] theories. We used a Green's function which incorporates causality and is valid for early arriving photons (Refs. 18 and 19). This Green's function is constructed from the diffusion approximation Green's function $G(\mathbf{r}, t|\mathbf{r}_0, t_0)$ by replacing the time t_0 at which the pulse is injected into the medium with $t_0 + t_{tr}$, with t_{tr} the time of flight for unscattered photons to propagate from the source to the detector. Physically, this procedure takes into account the fact that diffusion starts only after the light pulse traverses the medium.

Figure 6 shows the point spread functions calculated with the diffusion approximation solution and with the causality corrected solution. Note that all contour maps in Figure 6 correspond to the time window of the experimental data for the two object case.

The image reconstruction results for the x ray (straight line PSF), diffusion approximation, causality correction, and the actual configuration are presented in Figures 7 and 8. Figures 7 and 8 are 3D contour plots. Figure 9 presents characteristic slices of Figure 8(c) in 2D contour maps. The slices are picked at planes $z = -10$, -6, 2, and 10 mm. As clearly seen in Figures 7 and 8, the images reconstructed with the straight line path (x-ray CT) do not have high resolution, while the images reconstructed with the diffusion approximation are too small compared with the actual size of the spheres, especially for the two object case, in which the smaller object is invisible. Due to the noise in the experimental data, the reconstructed images for the one object configuration exhibit some distortions. Remarkably, for the two object configuration the image reconstructed with the causality correction gives correct sizes for the embedded objects. As shown in Figure 9, the voxel values off the objects are nearly zero, which naturally results from the inverse procedure. In Figure 8(c), the size and the position of the 8 mm object and the size of the 6 mm object are correct, while the position of the 6 mm object is off from its actual position by 2 mm. This may indicate that crosstalk exists in the inverse when two objects are embedded.

One of our findings is that the point spread function calculated with the conventional diffusion approximation solution is too wide for the early time window of our data. The reconstructed images in this case are too small compared with the actual size of the objects. This is especially true for the two object configuration where the smaller absorber is basically invisible in the reconstructed image. On the other hand, the same calculations done with the causality correction give much better results. This is clear evidence that correct image reconstruction with early time detection requires a theory beyond the diffusion approximation.

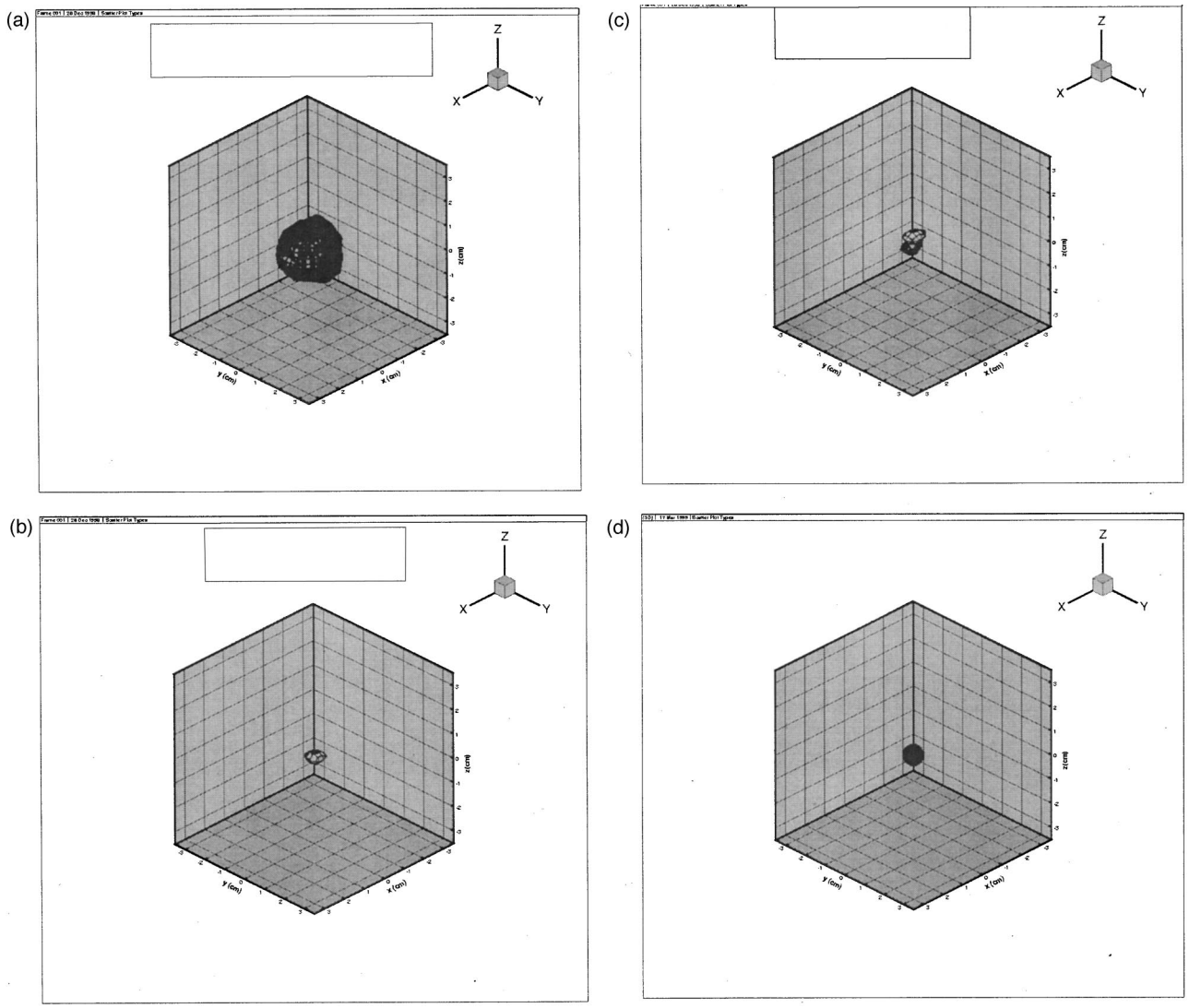

Fig. 7 Reconstructed images for one embedded object. (a) Reconstruction with the direct x-ray algorithm; (b) reconstruction with the diffusion approximation; (c) reconstruction with the causality correction; (d) the exact configuration. Due to noise in the data, the reconstructed images have some distortions.

6 Discussion and Conclusion

In the optical regime, the early arriving photons are analogous to x-ray photons. They undergo a smaller number of scattering events compared with highly diffusive photons, and thus preserve a significant amount of spatial information. Yet signal levels for early arriving photons can be relatively high. The experimental data taken using early time detection have higher resolution compared to those obtained with cw and frequency-domain techniques. An algorithm can be built by extending the x-ray algorithms to the regime of early arriving photons. Sharp images can be reconstructed using the concept of photon path density. The choice of model used to calculate the photon paths is very important. As is well known, the diffusion approximation solution does not describe the early arriving photons well. Our results show that predictions of the diffusion approximation for the point spread function up to the $t-t_0 \approx 600$ ps time window are inadequate for correct image reconstruction. A point spread function that takes into account causality produces much better results. The correct form of the point spread function for early time plays an essential role in image reconstruction.

The image reconstruction method presented in this article is based on extension of the x-ray CT series expansion method to the optical regime, where scattering is dominant and the distribution of photon paths between the source and detector must be taken into account. To accomplish this, we use the PSF to generate a weighting function matrix. In past work, weighting functions have been discussed and calculated using the diffusion approximation,[26] microscopic Beer–Lambert law,[9] and Monte Carlo simulations.[13,14] However, the use of the PSF provides valuable insight into the choice of weighting functions. The physical interpretation is clearer in terms of the PSF, and different theories of photon migration can be tested because they predict different PSFs. Furthermore, as shown in Eq. (12), there are actually two sets of

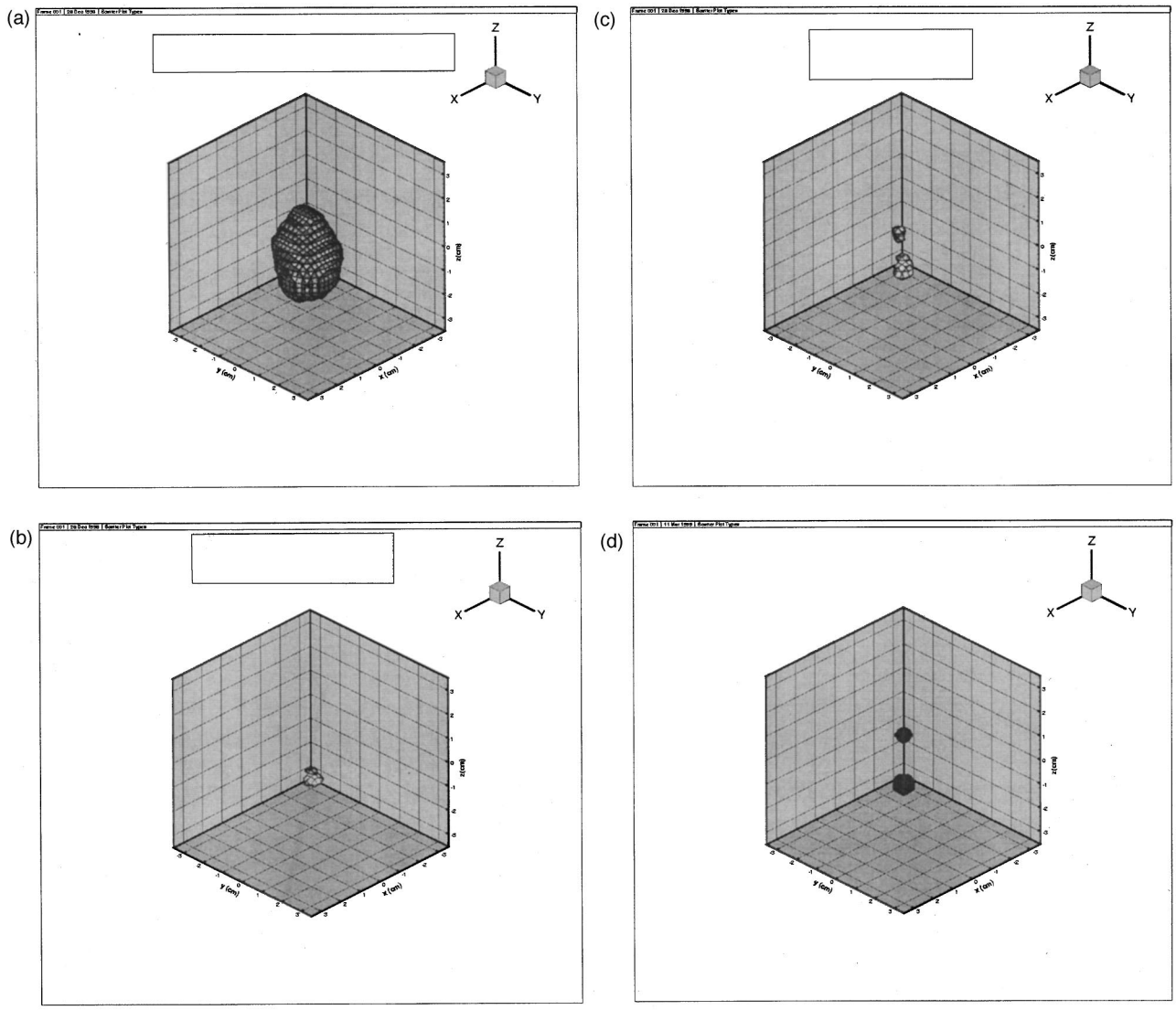

Fig. 8 Reconstructed images for two embedded objects. (a) Reconstruction with the direct x-ray algorithm; (b) reconstruction with the diffusion approximation; (c) reconstruction with the causality correction; (d) the exact configuration. Reconstruction with the direct x-ray algorithm does not resolve the two embedded objects. On the other hand, the reconstructions with the diffusion approximation overdo the deconvolution and result in smaller images. The smaller object is invisible in the 3D view.

weighting functions, one for scattering contrast and one for absorption contrast. In this article we only considered absorption-based contrast. However, tumors in breast tissue can exhibit both absorption and scattering contrast. The early portion of the photon migration curve is more sensitive to the scattering contrast than the absorption contrast. The extension of our algorithm to scattering contrast [Eq. (12)] is straightforward.

The resolution of optical CT is restricted by several factors, such as the effects of scattering and the underdetermined nature of the reconstruction procedures. In this article we have concentrated on establishing fundamental concepts of optical CT, with emphasis on early time detection and correct choice of the PSF. Although we successfully reconstructed 9261 voxel values from a total of 882 measurements of 2 projections, further technical improvements can be made after the fundamentals of optical CT are clear. For example, the total number of projections and measurements can be increased, and a fan-beam geometry[14,27] can be used to improve data collection efficiency. Refined time-domain photon migration instruments, implemented with correct reconstruction algorithms, have the potential to provide optical CT images of high quality in the breast, the brain, and perhaps elsewhere in the body.

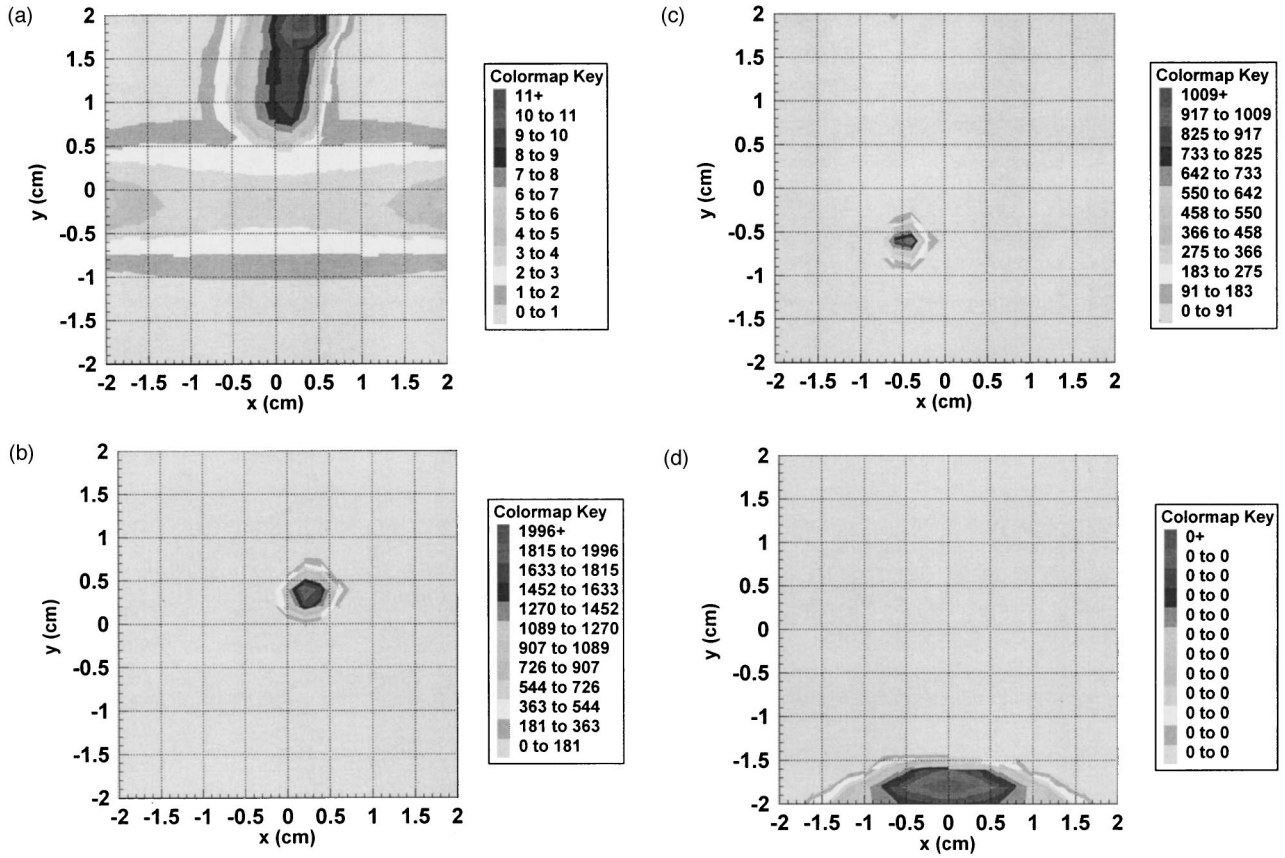

Fig. 9 Contour map diagram of four slices of the reconstructed image in Fig. 8(c). The slices are z= (a) −10, (b) −6, (c) 2, and (d) 10 mm.

Acknowledgments

This research was carried out at the MIT Laser Biomedical Research Center, supported by NIH Grant No. P41-RR02594. It was also partly supported by Hamamatsu Photonics Systems.

References

1. J. F. Evensen, S. Sommer, J. Moan, and T. Christensen, ''Tumor-localizing and photosensitizing properties of the main components of hematoporphyrin derivative,'' *Cancer Res.* **44**, 482–486 (1986).
2. M. A. O'Leary, D. A. Boas, B. Chance, and A. G. Yodh, ''Experimental images of heterogeneous turbid media by frequency-domain diffusing-photon tomography,'' *Opt. Lett.* **20**, 426–428 (1995).
3. H. Jiang, K. D. Paulsen, U. L. Osterberg, and M. S. Patterson, ''Frequency-domain optical image reconstruction for breast imaging: Initial evaluation in multitarget tissuelike phantoms,'' *Med. Phys.* **25**, 183–193 (1998).
4. K. Chen, L. T. Perelman, R. R. Dasari, and M. S. Feld. ''Optical tomographic imaging using fluorescence photon migration,'' *Proc. THICOLS'97*, pp. 421–426, Hangzhou, China (June 1997).
5. J. C. Hebden, D. J. Hall, M. Firbank, and D. T. Delpy, ''Time-resolved optical imaging of a solid tissue-equivalent phantom,'' *Appl. Opt.* **34**, 8038–8047 (1995).
6. J. C. Hebden and S. R. Arridge, ''Imaging through scattering media by the use of an analytical model of perturbation amplitudes in the time domain,'' *Appl. Opt.* **35**, 6788–6796 (1996).
7. S. B. Colak, D. G. Papaioannou, G. W. t'Hooft, M. B. van der Mark, H. Schomberg, J. C. J. Paasschens, J. B. M. Melissen, and N. A. A. J. van Asten, ''Tomographic image reconstruction from optical projections in light-diffusing media,'' *Appl. Opt.* **36**, 180–219 (1997).
8. X. D. Li, T. Durduran, A. G. Yodh, B. Chance, and D. N. Pattanayak, ''Diffraction tomography for biomedical Imaging with diffuse-photon density waves,'' *Opt. Lett.* **22**, 573–575 (1997).
9. H. Zhang, M. Miwa, Y. Yamashita, and Y. Tsuchiya, ''Quantitation of absorbers in turbid media using time-integrated spectroscopy based on microscopic Beer–Lambert law,'' *Jpn. J. Appl. Phys., Part 1* **37**, 2724–2727 (1998).
10. S. R. Arridge and M. Schweiger, ''Photon-measurement density functions. Part 2: Finite-element-method calculations,'' *Appl. Opt.* **34**, 8026–8037 (1995).
11. B. W. Pogue, M. S. Patterson, H. Jiang, and K. D. Paulsen, ''Initial assessment of a simple system for frequency domain diffuse optical tomography,'' *Phys. Med. Biol.* **40**, 1709–1729 (1995).
12. G. T. Herman, *Image Reconstruction From Projections: The Fundamentals of Computerized Tomography*, Academic, New York (1980).
13. R. L. Barbour, H. L. Graber, J. Lubowsky, R. Aronson, B. B. Das, K. M. Yoo, and R. R. Alfano, ''Imaging of diffusing media by a progressive iterative backprojection method using time-domain data,'' *Proc. SPIE* **1641**, 21–34 (January 1992).
14. H. Eda, I. Oda, Y. Ito, Y. Wada, Y. Oikawa, Y. Tsunazawa, M. Takada, Y. Tsuchiya, Y. Yamashita, M. Oda, A. Sassaroli, Y. Yamada, and M. Tamura, ''Multi-channel time-resolved optical tomographic imaging system,'' *Rev. Sci. Instrum.* **70**, 3595–3602 (1999).
15. L. T. Perelman, J. Wu, I. Itzkan, and M. S. Feld, ''Photon migration in turbid media using path integrals,'' *Phys. Rev. Lett.* **72**, 1341–1344 (1994).
16. L. T. Perelman, J. Winn, J. Wu, R. R. Dasari, and M. S. Feld, ''Photon migration of near-diffusive photons in turbid media: a Lagrangian-based approach,'' *J. Opt. Soc. Am. A* **14**, 224–229 (1997).
17. J. Winn, L. T. Perelman, K. Chen, J. Wu, R. R. Dasari, and M. S. Feld, ''Distribution of the paths of early-arriving photons traversing a turbid medium,'' *Appl. Opt.* **37**, 8085–8091 (1998).
18. A. H. Gandjbakhche, R. Nossal, and R. F. Bonner, ''Resolution limits for optical transillumination of abnormalities deeply imbedded in tissues,'' *Med. Phys.* **21**, 185–191 (1994).
19. V. Chernomordik, R. Nossal, and A. H. Gandjbakhche, ''Point spread functions of photons in time-resolved transillumination experiments

using simple scaling arguments,'' *Med. Phys.* **23**, 1857–1861 (1996).
20. A. Ishimaru, *Wave Propagation and Scattering in Random Media*, Academic, Orlando, FL (1978).
21. R. C. Haskell, L. O. Svaasand, T. Tsay, T. F. M. S. McAdams, and B. J. Tromberg, ''Boundary conditions for the diffusion equation in radiative transfer,'' *J. Opt. Soc. Am. A* **11**, 2727–2741 (1994).
22. See, for example, P. M. Morse and H. Feshbach, *Methods of Theoretical Physics*, pp. 858–859, McGraw–Hill, New York (1953).
23. M. S. Patterson, B. Chance, and B. C. Wilson, ''Time resolved reflectance and transmittance for the noninvasive measurement of tissue optical properties,'' *Appl. Opt.* **28**, 2331–2336 (1989).
24. S. Arridge, ''Photon-measurement density functions. Part I: Analytical forms,'' *Appl. Opt.* **34**, 7395–7409 (1995).
25. G. T. Herman, ''X-ray-computed tomography—Basic principles,'' in *Three-Dimensional Biomedical Imaging*, edited by R. A. Robb, Ed., Vol. 1, pp. 61–80, Chemical Rubber, Boca Raton, FL (1985).
26. V. Ntziachristos, X. Ma, and B. Chance, ''Time-correlated single photon counting imager for simultaneous magnetic resonance and near-infrared mammography,'' *Rev. Sci. Instrum.* **69**, 4221–4233 (1998).
27. J. C. Hebden, F. E. W. Schmidt, M. E. Fry, M. Schweiger, E. M. C. Hillman, D. T. Delpy, and S. Arridge, ''Simultaneous reconstruction of absorption and scattering images using multi-channel measurement of purely temporal data,'' *Opt. Lett.* **24**, 534–536 (1999).